# Understanding the nanoscale chemistry of as-received and fast neutron irradiated $Nb_3Sn$ RRP® wires using Atom Probe Tomography

L Wheatley[1], T Baumgartner[2], M Eisterer[2], S Speller[1], M P Moody[1], C R M Grovenor[1]
[1]Department of Materials, University of Oxford, Parks Road, Oxford, OX1 3PH
[2]Atominstitut, Vienna University of Technology, Stadionellee 2, 1020 Vienna, Austria

Received xxxxxx
Accepted for publication xxxxxx
Published xxxxxx

**Abstract**

Atom Probe Tomography has been used to study the effect of fast neutron irradiation on the local chemistry of $Nb_3Sn$ samples. Two RRP® wires doped with 2 at% Ti were analysed, one in the as-received condition and the other irradiated to a neutron fluence (E>0.1MeV) of $2.82x10^{22}$ $m^{-2}$ in the TRIGA-II reactor. The irradiated sample had a reduced $T_c$, an increase in $F_p$, a shift in the peak of the $F_p$ curve suggesting the introduction of secondary point pinning, and an increase in the estimated scaling field $B^*$. Atom Probe Tomography analysis has shown that polycrystalline $Nb_3Sn$ has three distinct regions of composition, near stoichiometry $Nb_3Sn$ (low Nb), regions with a higher Nb content than expected in equilibrium $Nb_3Sn$ (high Nb) and grain boundaries. The summed composition of these three regions lies within the $Nb_3Sn$ phase for both the as-received and irradiated samples. The distinct regions of high Nb $Nb_3Sn$ demonstrate incomplete diffusion in the as-received sample, and the reduction in volume of these high Nb regions after irradiation implies significant radiation induced diffusion has occurred. The presence of other features in the atomic-scale chemistry, such as the extent of Cu segregation at grain boundaries, three types of dislocation array, and unreacted Nb nanoparticles, are compared between samples.

Keywords: $Nb_3Sn$, Atom Probe Tomography, neutron irradiation, restacked-rod-processed, composition

## 1. Introduction

Demand for $Nb_3Sn$ superconducting wire has increased in recent years, having been selected for both major nuclear fusion and particle accelerator applications [1, 2, 3]. At the same time, efforts have been made to improve the superconducting performance of commercial materials. Since the 1970s it has been shown that controlling the composition and doping in the $Nb_3Sn$ phase is important for maximising $J_c$ [4]. The equilibrium $Nb_3Sn$ phase exists over a range of compositions between 18-25 at% Sn [5], and achieving a composition as close to 25 at% as possible has been shown to increase $B_{c2}$ and $T_c$ values [6]. In the 1980s the addition of Ti and/or Ta was shown to increase $B_{c2}$ of $Nb_3Sn$ [7]. There has been debate in the literature as to where the Ti and Ta substitute in the $Nb_3Sn$ lattice, with recent confirmation using EXAFS showing that Ti substitutes only onto the Nb sites whereas the Ta substitutes onto both Nb and Sn sites [8]. Cu, which is added to $Nb_3Sn$ to lower the temperature of reaction and also act as a cryostabiliser, has been seen to segregate strongly to the grain boundaries in $Nb_3Sn$ [9, 10] with little or no solubility of Cu observed in the $Nb_3Sn$ grains [11]. By contrast, Ti has shown some solubility within $Nb_3Sn$ grains, weakly segregating to grain boundaries in bronze processed $Nb_3Sn$ wires [10, 12].

 

For applications such as fusion reactors and particle accelerators where magnets will be subjected to irradiation during their service lifetime, it is important to understand how irradiation affects the superconducting properties of $Nb_3Sn$. Fast neutron irradiation was studied during the 1970s on older generations of $Nb_3Sn$ wires [13, 14, 15, 16]. The neutron flux was shown to introduce regions of disorder which increase in number as the fluence increases. This disorder has been suggested to include point defects such as vacancies, interstitials and Frenkel pairs which can reduce the local order. Agglomeration of these sub-nanoscale point defects can produce visible nanoscale regions which have been detected by TEM and HR-STEM studies on neutron irradiated $Nb_3Sn$ wires [17, 18, 19, 20]. These larger regions of disorder are approximately 2-10 nm in size, but there is no clear agreement on their exact nature. For samples irradiated in the neutron spectrum from the TRIGA-II reactor an average diameter of 2 nm has been predicted for these disordered regions through energy displacement calculations [21]. As the neutron dose increases the number density of disordered regions increases, such that the distance between the disordered regions reduces. When the separation distance starts to approach the coherence length there is a reduction in $T_c$ [14].

Dew-Hughes developed theoretical models of different types of pinning mechanisms for type II superconductors, which can be identified by the shape of their pinning force curves. In polycrystalline $Nb_3Sn$ the dominant mechanism for pinning fluxons is surface pinning at grain boundaries [22]. However, in neutron irradiated $Nb_3Sn$ as well as an increase in the overall pinning force ($F_p$), the peak in the pinning force curves have often been shown to shift from the position of characteristic grain boundary pinning towards that of point pinning [21]. In the point pinning model suggested by Dew-Hughes, the maximum pinning occurs when the defect size is double the coherence length [22]. In $Nb_3Sn$ the coherence length is ~3-4 nm so it is plausible that the defects seen in TEM and HR-STEM experiments are contributing to this additional flux pinning.

However, using current electron microscopy tools it is challenging to determine whether neutron irradiation could also be producing local changes in the nanoscale chemistry of the $Nb_3Sn$ microstructure. Atom Probe Tomography (APT) is a 3D characterisation technique offering < 1nm spatial resolution and sensitivity down to parts per million [23]. Although the microstructural volumes sampled by each APT analysis are relatively small, because of the fine grain size in $Nb_3Sn$ wires, a typical APT reconstruction can incorporate several grains (and thus capture multiple grain boundaries). The first report of APT analysis on $Nb_3Sn$ wires in 2013 [10] showed grain boundary segregation of Cu and Ti, quantified using the principle of Gibbsian excess at grain boundaries. More recently APT has been used to look at the size distribution and number density of nanoscale $HfO_2$ and $ZrO_2$ pinning centres in $Nb_3Sn$ [24, 25] and to investigate the concentrations of species at the $Nb/Nb_3Sn$ interface in an internally oxidised $Nb_3Sn$ wire doped with Zr and O [26]. However APT analysis has not yet been applied to the characterisation of commercial RRP® wires nor any form of irradiated $Nb_3Sn$ wires. In this work the nanoscale structure of as-received and neutron irradiated $Nb_3Sn$ RRP® wires will be presented and discussed in the light of their $T_c$, $J_c$ values, and $F_p$ curves. The aim is to understand how changes to the nanoscale chemistry of the irradiated wires may be affecting the superconducting properties.

# 2. Experimental Details

### 2.1 Samples, $T_c$ and $J_c$ measurements

The two wires analysed in this work were Bruker-OST RRP® wires doped with 2 at% Ti and heat treated at 210°C for 48 hrs, 400°C for 48 hrs and finally 665°C for 50 hrs. One wire was analysed as-received and the other was irradiated to a fast neutron fluence (E > 0.1 MeV) of $2.82 \times 10^{22}$ $m^{-2}$ in the TRIGA-II reactor. Further details on the irradiation can be found in S. Pfeiffer's work [20]. The irreversible magnetic moment ($m_{irr}$) and $J_c$ values were calculated from the Bean critical state model from data measured using a Quantum Design MPMS XL SQUID magnetometer on 4 mm long wire samples with B perpendicular to the axis of the wire as described by Baumgartner *et* al [27]. $J_c$ values were measured at 12 different temperatures (4.2, 5, 6…, 15 K) using field steps of 0.2 T up to 7 T. $T_c$ was calculated from AC susceptibility measurements using a frequency of 30 Hz and 30 μT, and taken as the mid-point of the superconducting to normal transition in the susceptibility curve [27].

### 2.2 Determining $\chi$ and $F_p$

To produce the susceptibility ($\chi$) curve from AC magnetisation ($m_{ac}$) data, $\boldsymbol{\chi = \frac{1}{1-D_m}\frac{m_{ac}\mu_0}{BV}}$ where $D_m$ is the demagnetising factor (0.5 for a transversal cylinder), B = 30μT and V is the volume of each filament, approximated as a hexagon multiplied by the number of filaments (108). This result yielded $\chi$ values close to -1 below the superconducting transition. For simplicity, the data were scaled to set $\chi$ below the transition to -1.

To calculate the volume pinning force $\boldsymbol{F_p} = |\vec{\boldsymbol{B}} \times \overrightarrow{\boldsymbol{J_c}}|$, which is simplified to $F_p = J_c B$ because the applied field and irreversible currents are approximately perpendicular. For the as-received $Nb_3Sn$ sample, a good fit was obtained using Dew-Hughes's surface pinning model, equation 1. For the data from the irradiated sample, 100% grain boundary pinning did not give a good fit, so a weighted average of grain boundary and point pinning as shown in equation 2, was used based on previous work [21, 27, 28]. In both cases, B* as an approximation for $B_{c2}$, was extracted by fitting to the $F_p$ curve because resistivity measurements for this sample were unavailable to extract $B_{c2}$ directly.

$$\boldsymbol{F_{GB}} \propto \left(\frac{\boldsymbol{B}}{\boldsymbol{B_*}}\right)^{0.5}\left(\boldsymbol{1}-\left(\frac{\boldsymbol{B}}{\boldsymbol{B_*}}\right)\right)^{2} \quad (1)$$

$$\boldsymbol{F_{IRR}} \propto \boldsymbol{\alpha}\left(\frac{\boldsymbol{B}}{\boldsymbol{B_*}}\right)^{0.5}\left(\boldsymbol{1}-\left(\frac{\boldsymbol{B}}{\boldsymbol{B_*}}\right)\right)^{2} + \boldsymbol{\beta}\left(\frac{\boldsymbol{B}}{\boldsymbol{B_*}}\right)\left(\boldsymbol{1}-\left(\frac{\boldsymbol{B}}{\boldsymbol{B_*}}\right)\right)^{2} \quad (2)$$

To estimate a value for $B_{c2}(0)$ the temperature dependence of the upper critical field was fitted to equation 4, an approximation to the dirty limit dependence through an approximation to the dirty limit dependence of $B_{c2}$ by Helfand and Werthamer [29]. Here we assume B*(T) ~ $B_{c2}(T)$, using the constants $C_1 = 0.153$ and $C_2 = 0.152$ reported by Baumgartner *et al* [27].

$$\boldsymbol{h^*_{fit}}\left(\frac{\boldsymbol{T}}{\boldsymbol{T_c}}\right) = \left(\boldsymbol{1}-\frac{\boldsymbol{T}}{\boldsymbol{T_c}}\right) - \boldsymbol{C_1}\left(\boldsymbol{1}-\frac{\boldsymbol{T}}{\boldsymbol{T_c}}\right)^{2} - \boldsymbol{C_2}\left(\boldsymbol{1}-\frac{\boldsymbol{T}}{\boldsymbol{T_c}}\right)^{4} \quad (3)$$

$$\boldsymbol{B_{c2}(T)} = \frac{\boldsymbol{B_{c2}}}{\boldsymbol{0.693}}\boldsymbol{h^*_{fit}}\left(\frac{\boldsymbol{T}}{\boldsymbol{T_c}}\right) \quad (4)$$

### 2.3 Samples for Atom Probe Tomography

To reduce the activity of the samples, the irradiated wire was separated into subelements and placed on carbon tape, before transportation from Vienna, as shown in figure 1b. The grain size of the as-received sample has previously been measured to be 108 ± 48 nm [20], so there is a good chance of analysing several grain boundaries in a typical APT sample with a z dimension of several hundred nanometres, without the need for a more intensive site-specific specimen approach.

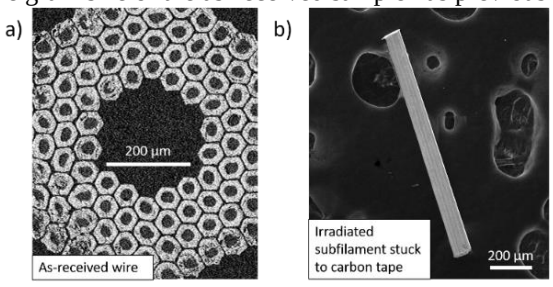


Figure 1. a) Cross-sectional image of an as-received RRP® wire doped with 2 at% Ti b) A subelement extracted from a 2 at% Ti RRP® wire irradiated to a neutron fluence of $2.82 \times 10^{22}$ $m^{-2}$

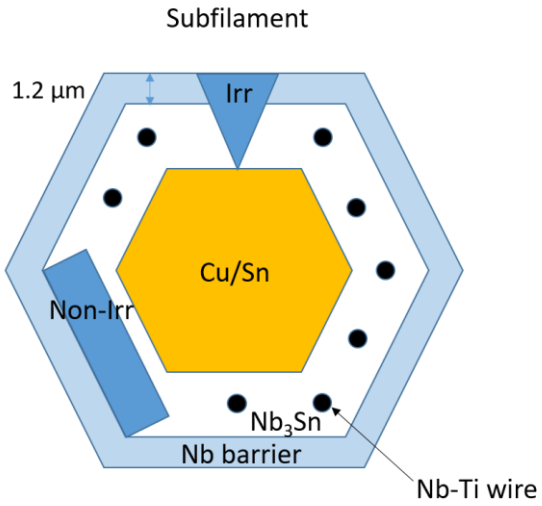


Figure 2. Geometry of a subelement of an RRP® wire. Samples were taken from the cross section of the as-received sample from a lift-out labelled 'Non-Irr'. Samples from the irradiated subelements, labelled 'Irr', had to be taken from the top, through the outer Nb barrier layer due to the geometry of the single subelements.

To produce APT tips from the as-received sample, a cross section of the wire was ground and polished and placed in a Zeiss Crossbeam Field Ion Beam (FIB) microscope. A standard liftout procedure was followed, with the APT samples mounted on silicon posts [23]. To extract APT tips from the irradiated subelements lift-outs were produced from the top of the subelements. To ensure all the outer Nb barrier layer was removed from the irradiated samples before shaping APT tips, EDX analysis was used to measure the amount of Nb which had to be milled away from the external surface of the subelement. In RRP® wires there has previously been shown to be a weak Sn gradient in concentration through the reacted $Nb_3Sn$ layer [30]. Taking this into account, APT needles from both the as-received and irradiated samples were taken from similar regions towards the outer edge of the $Nb_3Sn$ layer, and we expect them to have comparable Sn contents. The geometry of the lift-out locations can be seen schematically in figure 2.

### 2.4 Atom Probe Tomography Analysis Conditions

APT analysis was carried out on CAMECA LEAP 5000 XR and XS instruments, at a laser energy of 50 pJ, a temperature of 60 K, with a pulse frequency of either 125 kHz on the XR or 250 kHz on the XS and a detection rate of 0.3. To reconstruct the APT data, IVAS software was used with an evaporation field constant of 37 $Vm^{-1}$.

## 3. Results

### 3.1 $T_c$ and $J_c$ Measurements

The results from AC-susceptibility measurements can be seen in figure 3. The as-received sample had a $T_c$ of 17.6 K, and the irradiated sample showed a drop in $T_c$ to 16.6 K. The transition shown at ~8-9 K is the $T_c$ for Nb which forms the outer layer of each subelement.

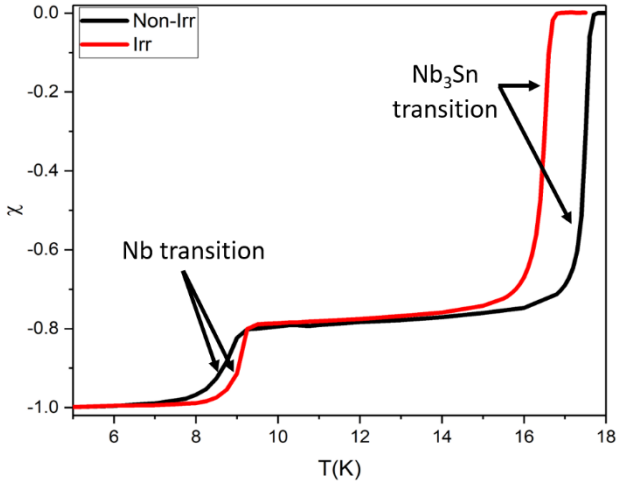


Figure 3. Susceptibility curves for the as received and irradiated $Nb_3Sn$ wire samples.

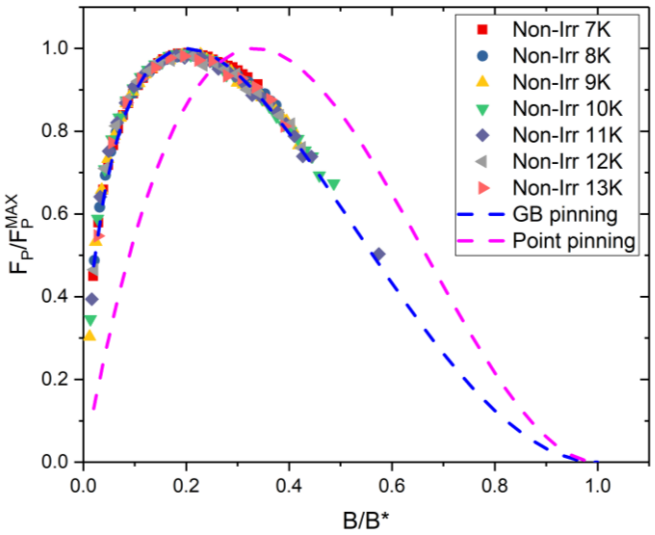


Figure 4. Plots of the as-received sample - normalised pinning force curves against reduced field. The as-received sample shows a good fit to the Dew-Hughes grain boundary pinning model.

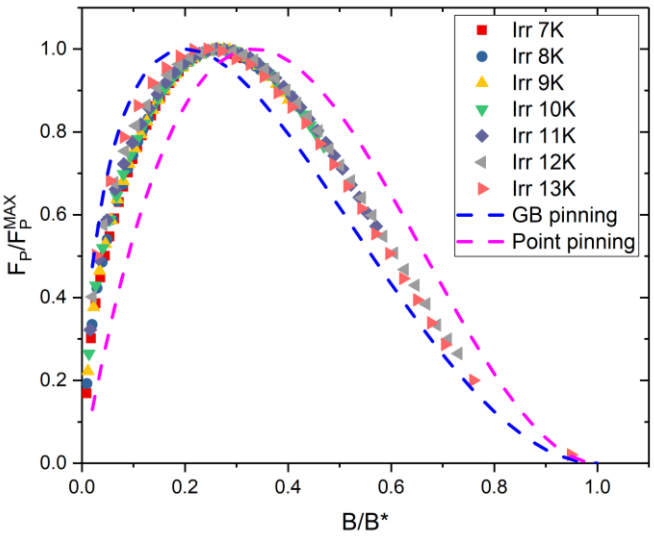


Figure 5. Plots of the irradiated sample - normalised pinning force curves against reduced field. The irradiated sample can be best fitted with a linear combination of grain boundary and point pinning models.

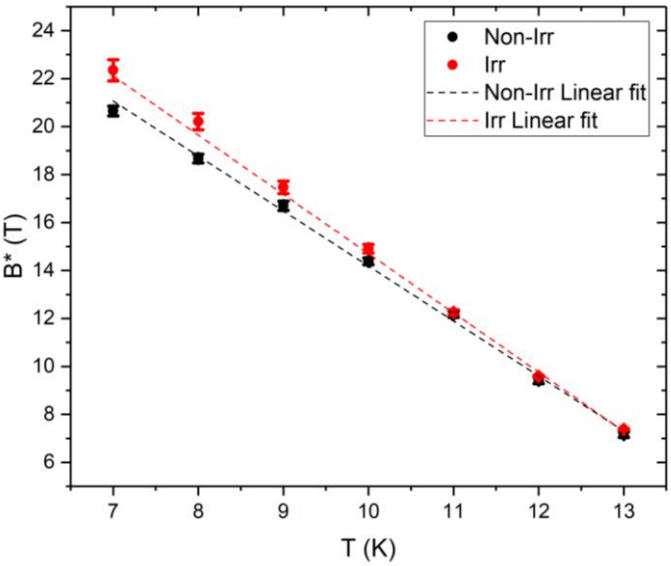


Figure 6. Plots of B* against temperature for both the irradiated and as-received sample. Error bars are estimates from the curve fitting, with higher uncertainty at lower temperatures due to the reduction in number of datapoints near $B_{c2}$.

Although data were available over a temperature range between 4.2 K and 15 K, only temperatures between 7-13 K were used to produce $F_p$ curves. At lower temperatures the peak pinning force was not reached in the 7 T field range of the measurements, and the higher temperature data had only a few measured values. Normalised pinning force curves for the as-received and irradiated samples over this temperature range were then plotted against the point pinning function and the grain boundary function, as seen in figures 4 and 5.

There is a clear shift in the normalised pinning force curve from 100% grain boundary pinning in the as-received sample to a mixture of grain boundary and point pinning in the irradiated sample, with a peak shift from 0.2 towards 0.3. There is also an increase in the magnitude of $F_p$ in the irradiated sample when using equations 1 and 2, for example at 4.2 K the peak pinning force for the as-received sample is 84.3 GN/m$^3$, increasing by 58% to 134 GN/m$^3$ for the irradiated sample. In figure 6 the calculated $B^*$ values are higher for the irradiated sample at lower temperatures, which has previously been reported for similar irradiated RRP® wires [28]. Based on the Helfand and Werthamer fit between 10 and 15 K, $B_{c2}(0)$ = 31.4 T for the as-received sample and $B_{c2}(0)$ = 32.5 T for the irradiated sample, an increase of 3.3% after irradiation. As a result of this analysis, we have used APT to seek explanations for the changes in superconducting properties as a result of neutron irradiation.

### 3.2 Results from Atom Probe Tomography

For the as-received sample 7 atom probe tips were successfully analysed incorporating 29 grain boundaries in total. For the irradiated sample 11 atom probe tips were analysed containing 27 grain boundaries. The total volume of the as-received tips sampled is approximately 8.6x10$^6$ nm$^3$ and the total volume of irradiated tips sampled is approximately 5.8x10$^6$ nm$^3$. Because the APT data is in the form of 3D chemical analysis at a sub-nanometre scale, specific regions within the reconstruction can be isolated enabling the analysis to focus specifically on $Nb_3Sn$ grains, grain boundaries and other features of interest.

#### 3.2.1 Intragrain $Nb_3Sn$ composition variations

$Nb_3Sn$, in its binary form, has a range of compositions from ~ 18-25 at% Sn [5], and there is normally a gradient of composition across the thickness of the reacted A15 layer [20, 31, 32]. The local composition within individual nanoscale grains has been difficult to probe in $Nb_3Sn$ wires, although one TEM study has presented an EDX profile across a single grain [20]. The profile showed a depletion in Nb at grain boundaries and then an increasing Nb content towards 80 at% the middle of the grain. To compare the composition of the A15 phase within individual grains of the as-received and irradiated samples in our APT data, iso-concentration surfaces (isosurfaces) were used to highlight regions of differing composition. Isosurfaces encapsulate a region of data with a concentration either above or below a user selected threshold e.g. an isosurface of 10 at% Cu can show any region of data ≥10 at% Cu or ≤10 at% Cu. Figure 7 shows a typical analysed volume from the as-received material with distinct regions of significantly differing Nb concentration inside individual $Nb_3Sn$ grains. Below we will define three regions in the $Nb_3Sn$; (1) grain boundaries, (2) (nearly) stoichiometric $Nb_3Sn$ regions within the grains which will be classified as *low Nb* and (3) regions within the $Nb_3Sn$ grains with a higher Nb content than predicted by the $Nb_3Sn$ phase diagram, which will be classified as *high Nb* regions.

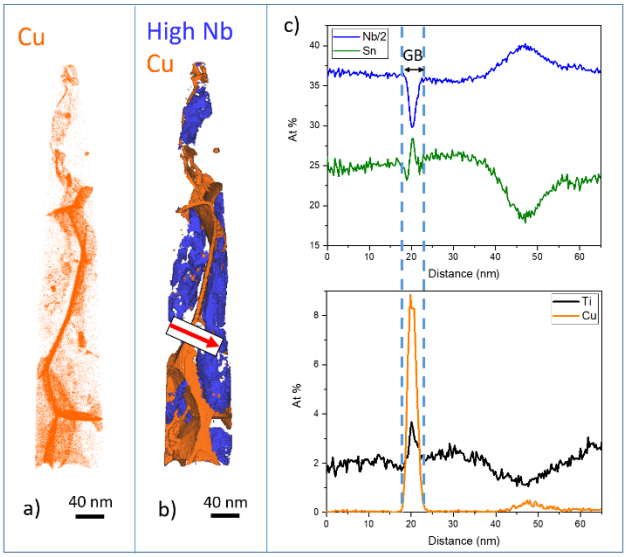


Figure 7. A typical APT analysis of the as-received material a) a Cu ion map highlighting the grain boundaries and additional regions of Cu segregation. b) A 2 at% Cu isosurface, with the surface enclosing any region ≥ 2 at% Cu and an 82 at% Nb isosurface to identify volumes of high Nb content inside the $Nb_3Sn$ grains with ≥ 82 at% Nb (the blue regions). c) A 1D concentration profile has been taken across a grain boundary in b) (red arrow) and into a high Nb region to show the variation in total local Nb/2, Sn, Ti and Cu concentrations.

| | Nb at% | Sn at% | Ti at% | Cu at% |
|---|---|---|---|---|
| **Non-Irr High Nb** | 83.7±0.9 | 16.0±0.8 | 0.2±0.1 | 0.1±0.1 |
| **Non-Irr Low Nb** | 73.1±0.6 | 25.5±0.8 | 1.4±0.4 | 0 |
| **Irr High Nb** | 85.5±1.2 | 14.1±1.3 | 0.1±0.1 | 0.3±0.2 |
| **Irr Low Nb** | 73.2±0.6 | 25.5±0.8 | 1.3±0.4 | 0 |

Table 1. Average compositions of the regions of high and low Nb in the as-received and irradiated samples with their associated standard deviations.

Regions of interest (ROIs) were defined and used to isolate discrete volumes of $Nb_3Sn$ with high and low Nb for further analysis from APT datasets from both the as-received and the irradiated samples. The resulting composition measurements are displayed in figure 8. This figure presents the measured subvolume compositions on a Nb-Sn-Ti ternary composition map. For comparison, also presented is the ternary equilibrium existence range of the A15 phase from Flükiger *et al* [6]. It is apparent that both the as-received and irradiated materials contain regions respectively defined by two distinct Nb:Sn ratios for low and high Nb, as summarised in table 1. Furthermore, it is shown that Ti is segregated strongly to the low Nb regions in both the as-received and irradiated samples, as expected from the expectation of an excess vacancy concentration on the Nb sublattice and the EXAFS results showing that Ti lies on the Nb sites [8]. The average Nb+Ti compositions for the as-received sample are 74.5 at% in the low Nb regions and 83.8 at% in the high Nb regions – which emphasises that especially the high Nb regions do not lie within the equilibrium $Nb_3Sn$ existence range. The average compositions of the entire analysed volumes have also been extracted, using the methodology described in 3.2.4, and in both materials these values do lie within the existence range

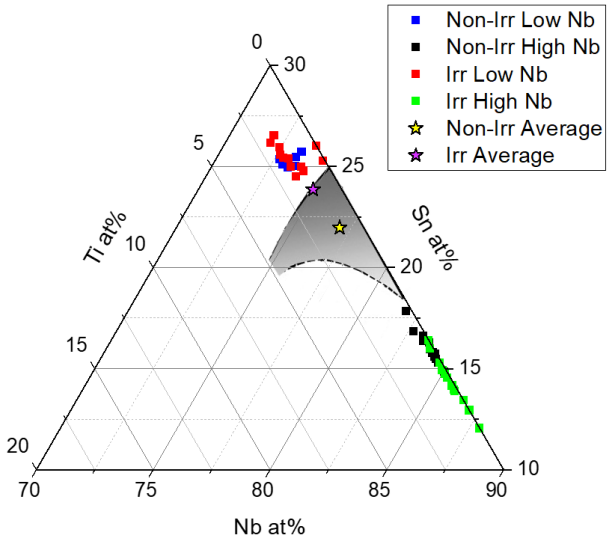


of the A15 compound.

Figure 8. A ternary composition map of the regions of high and low Nb content $Nb_3Sn$ within individual grains of both the as-received and irradiated samples. The phase field of the ternary Nb-Sn-Ti A15 phase from [6] has been superimposed on the ternary phase map, with the average compositions of the as-received and irradiated samples (shown as stars) lying within the existence range of the A15 compound.

### 3.2.2 Grain Boundary Analysis – Gibbsian Interfacial Excess

A typical grain boundary concentration profile extracted from an as-received sample can be seen in figure 7, where each boundary shows segregation of Cu, Ti, a significant decrease in Nb concentration and some boundaries have Sn segregation to the boundary. Previous work using Auger spectroscopy and APT has demonstrated similar changes in grain boundary composition within bronze-processed wires [9, 10]. To quantify the amount of Cu solute at the grain boundary, the method of Gibbsian interfacial excess ($\Gamma_i$) has been employed. $\Gamma_i$ is defined by equation 5 where $\mathbf{N_i^{excess}}$ is the excess number of counts of solute i at the interface, $\eta$ is the detection efficiency of the relevant LEAP5000 instruments, and A is the area of the interface sampled.

$$\mathbf{\Gamma_i = \frac{N_i^{excess}}{\eta A}} \qquad (5)$$

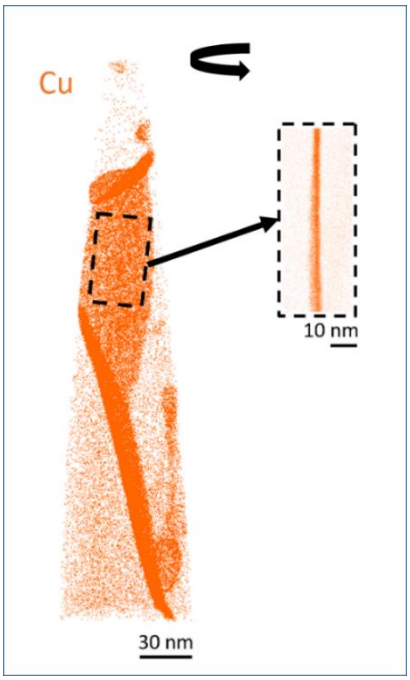


Figure 9. Atom probe reconstruction of a tip from an as-received sample showing only the Cu ions. An ROI has been used to isolate one of the grain boundaries.

To quantify the amount of excess solute, in the first step, the analysis was confined to an ROI incorporating the interface, as shown in figure 9. Then the excess was calculated using R-code software [33]. Gibbsian excess analysis uses a 1D concentration profile across the grain boundary to produce the excess atoms. Care was taken to make sure that each ROI was aligned perpendicular to the grain boundaries to minimise blurring of the 1D solute peaks.

Measurements of the Gibbsian excess of Cu were calculated across grain boundaries for both samples, respectively, and plotted as a probability density diagram in figure 10. The height on the y-axis provides a measure of how likely a specific excess value is, and the width of the curve relates to the standard deviation of the data. The irradiated sample has a mean value of excess Cu atoms/nm$^2$ at the grain boundaries which is marginally higher than in the as-received sample, but with a significantly wider distribution of values. This suggests that the irradiation does result in some modification of the behaviour of Cu in these samples. The Gibbsian excess was not used as a measurement for excess Ti at the grain boundaries because, as shown in figure 7, Ti shows such weak segregation to the boundaries, that much larger errors are introduced when selecting precisely the start and the finish of the segregation profile to implement the measurement. However, although weakly, it is still clear that Ti does segregate to the grain boundaries in both samples.

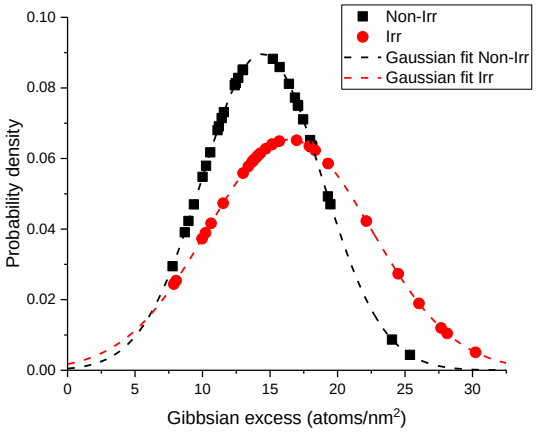


Figure 10. Probability density diagram of the Gibbsian excess values of Cu at grain boundaries in the as-received and irradiated samples.

### 3.2.3 Additional features of interest

The as-received sample contained a significant number of small Nb-rich particles and dislocations highlighted by segregated Cu. Three tips from the as-received sample contained nanoparticles of almost pure Nb like those shown in figure 11. The line profile across the largest of these also shows strong segregation of Cu to the interface with the A15 matrix. We suppose that these are likely to be residual unreacted Nb from the original Nb rods, and have been previously been identified in Ti RRP® wires using STEM/EDX [20]. In the APT specimens analysed from the as-received sample there were 7 Nb particles similar to those seen in figure 11, whereas the irradiated samples analysed only contained 3 Nb clusters. The size of these Nb clusters also varied significantly between the as-received and irradiated material, as shown in figure 12. The size, by measure of 3D volume, of the Nb clusters is far larger in the as-received sample, with the mean volume of a cluster being 2350 nm$^3$ compared to 260 nm$^3$ in the irradiated material. However, statistically there are very few clusters present in either sample, therefore care should be taken to not over interpret this volume difference.

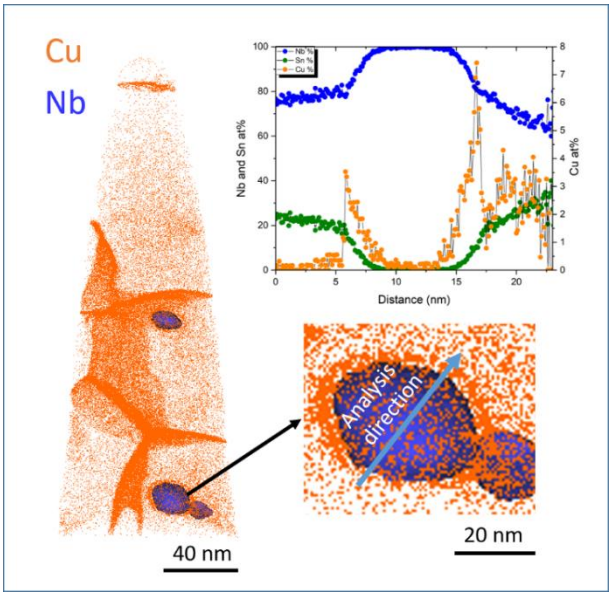


Figure 11. Atom probe reconstruction of a $Nb_3Sn$ tip from the as-received material showing Nb-rich particles identified by the 95 at% Nb iso-concentration surface (and a line profile across one of the particles).

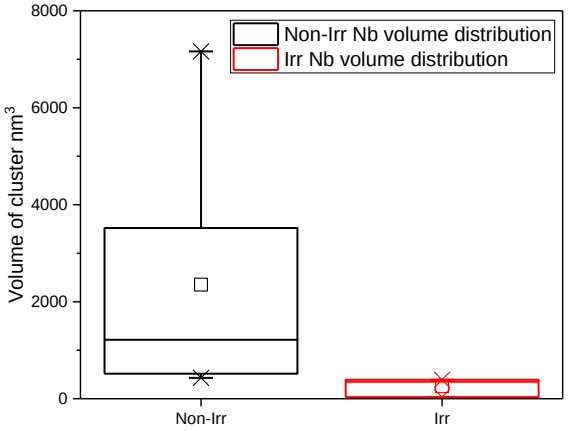


Figure 12. Box plot showing the volume of each Nb cluster in the as-received and irradiated samples

Dislocations highlighted by Cu atoms could be seen in five different samples from the as-received material. Two types of dislocation can be observed in the as-received sample. The first take the form of regular arrays of line dislocations which appear to constitute a low angle grain boundary, as shown in figure 13. The second type are individual dislocations extending out of the plane of the grain boundary. Similar Cu segregation to dislocations was seen in the irradiated material, but arrays consisting of two orthogonal sets of dislocations were also found as shown in figure 14. A third type of dislocation has been seen in the irradiated sample, this is a dislocation loop revealed by segregation of Cu, as shown in figure 15. Dislocation loops with a diameter of 15 to 30 nm have previously been seen in fast neutron irradiated $Nb_3Sn$ tapes using TEM [19], and they are commonly seen in neutron irradiated nuclear structural materials like steels and Zr alloys [34].

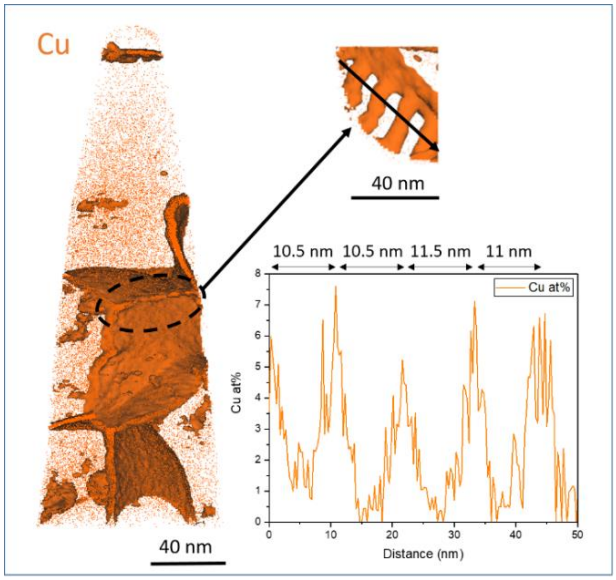


Figure 13. Atom probe reconstruction of an as-received $Nb_3Sn$ tip showing Cu atoms and a 2 at% Cu isosurface. Down the axis of the tip the dislocation features enriched in Cu can be extracted and a line profile of the Cu drawn across the dislocations.

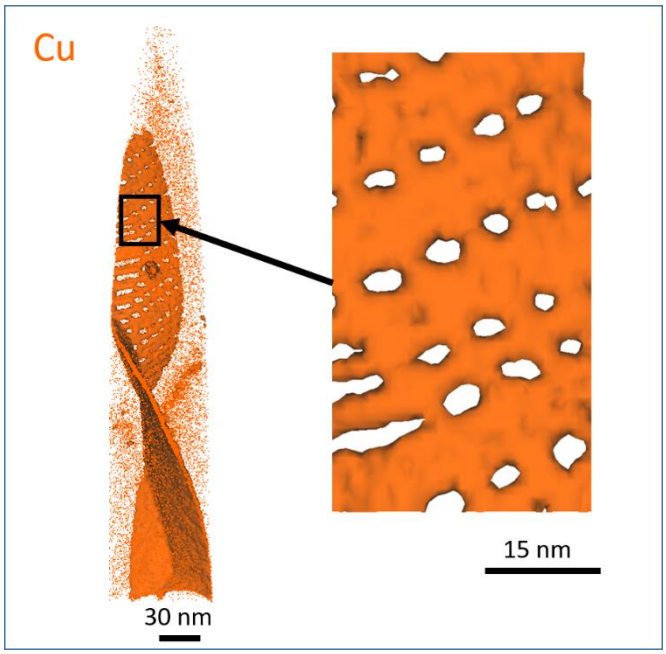


Figure 14. Atom probe reconstruction of a grain boundary in an irradiated tip. The boundary contains an orthogonal array of dislocations decorated with Cu. The boundary is highlighted with a 2 at% Cu isosurface.

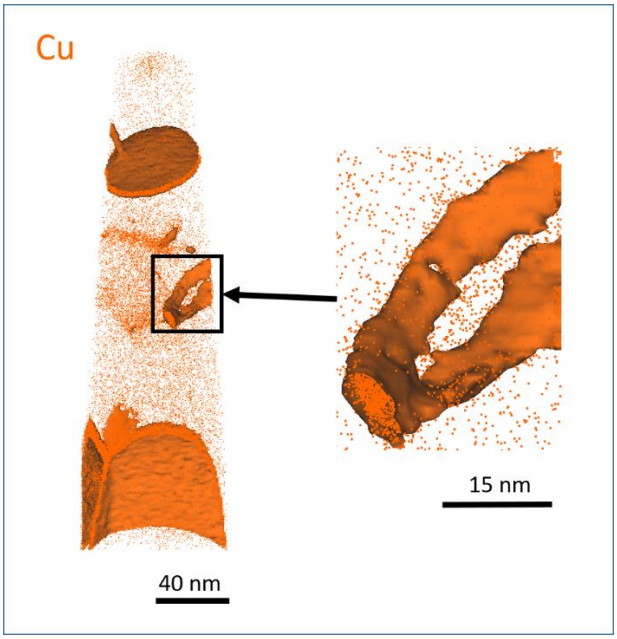


Figure 15. Atom probe reconstruction of a dislocation loop in an irradiated tip. The loop is 'hoop' shaped and highlighted with a 2 at% Cu isosurface.

#### 3.2.4 Volume of regions of differing composition

To determine if the overall compositions of the as-received and irradiated material lie within the expected $Nb_3Sn$ composition range, the volume and composition of each region (high Nb, low Nb and grain boundaries) were extracted and an overall average composition calculated. The grain boundary composition was extracted from the Gibbsian excess calculation, which gave a composition between the edges of a user defined interface, and the volume fraction of the grain boundaries was extracted using a ≥2 at% Cu isosurface. The volume fraction of high Nb regions were defined by a ≥80 at% Nb isosurface. Any additional areas of interest, such as the pure Nb particles, were extracted with a ≥95 at% Nb isosurface. The volume fraction left over after the grain boundaries, high Nb regions and Nb particles were extracted constituted the low Nb regions.

The average composition for the as-received and irradiated sample was calculated using equation 6 for each species, x= Nb,Sn,Ti,Cu, where C is the concentration in at%, $V_f$ is volume fraction of each region and the error was given as $\sqrt{\sigma^2{}_{Low} + \sigma^2{}_{High} + \sigma^2{}_{GB}}$ .

$$\boldsymbol{C_x(at\%) = \left(C_x^{High\ Nb} \times V_f^{High\ Nb}\right) + \left(C_x^{Low\ Nb} \times V_f^{Low\ Nb}\right) + \left(C_x^{GB} \times V_f^{GB}\right)} \quad (6)$$

The average compositions for the as-received material were: $C_{Nb}$ = 74.5 ± 3.6 at%, $C_{Sn}$ = 23.8 ± 2.0 at%, $C_{Ti}$ = 1.2 ± 0.9 at% and $C_{Cu}$ = 0.5 ± 1.5 at%. The irradiated material had an average composition of: $C_{Nb}$ = 76.6 ± 2.6 at%, $C_{Sn}$ = 21.9 ± 1.8 at%, $C_{Ti}$ = 1.0 ± 0.7 at% and $C_{Cu}$ = 0.5 ± 1.5 at %. These average compositions can be seen to lie within the predicted A15 phase field for ternary Nb-Sn-Ti, as shown in figure 8. If we assume that all the Ti substitutes onto the Nb lattice then the (Nb+Ti)/Sn ratio for the as-received sample is 3.6 and the ratio for the irradiated material is 3.2. This illustrates that nanoscale variation in composition within $Nb_3Sn$ grains can vary far more widely than predicted by the $Nb_3Sn$ equilibrium phase diagram.

The volume fraction of each type of region also varied in the as-received and irradiated materials. 37.2% of the analysed volume of the as-received material classified as high Nb, whereas the irradiated sample only had 14.8% of the volume with a high Nb concentration. The grain boundary volume only changed from 11.8% for the as-received sample to 9.7% for the irradiated sample, which is within what would be expected for random variations in a nanoscale microstructure.

# 4. Discussion

The superconducting results after irradiation show a decrease in $T_c$, an increase in $B_{c2}$, $J_c$, $F_p$ and a shift in the pinning force curve that suggests the introduction of additional point pinning. Despite the as-received and irradiated samples having been taken from different sections of the original RRP® wire, the superconducting results are similar to previous results on irradiated RRP® wires [27, 28].

The APT results above show that there are several features that might be contributing to this modification of the superconducting properties in the irradiated sample; regions of high Nb content, increased Cu segregation at grain boundaries, Nb nanoparticles and dislocation loops. Discrete volumes of high and low Nb content have been found within both the as-received and irradiated sample. The low Nb regions contain, within experimental detection limits, no Cu, but the high Nb regions show very low, but distinguishable amounts of Cu. Ti shows higher solubility in the low Nb regions than in the high Nb regions. In the low Nb regions, the (Nb+Ti)/Sn ratio, assuming all the Ti atoms lie on Nb sites, lies within the A15 phase field in the binary equilibrium Nb-Sn phase diagram. However, the same ratio from the high Nb regions lies outside the A15 existence area in figure 8, suggesting that there must be significant antisite disorder, with the excess Nb atoms lying on Sn sites ($Nb_{Sn}$). Off stoichiometry of the $Nb_3Sn$ structure is known to be dominated by antisite disorder [35], with the density of vacancies remaining negligible [36]. Work on SRF cavity materials using density functional theory to model antisite disorder in $Nb_3Sn$ has shown $Nb_{Sn}$ antisite defects cluster together to form tin-depleted regions at free surfaces [37]. The grain size in RRP® materials is so small that it is possible that the combination of the depletion of Nb at the grain boundaries shown in figure 7 and the resulting clustering of $Nb_{Sn}$ defects in the surrounding grains produce the observed regions of increased Nb concentration, and that they are kinetically stabilised by the very slow diffusion rate of Nb towards the grain boundaries even at the final reaction temperature.

However, the high Nb/Sn ratio could also be reduced by diffusion of Sn. Previous experiments using Kirkendell markers have shown that Sn is the fastest diffusing species in the A15 compound [38], despite first principles calculations predicting Nb as the faster diffusing species [36]. This discrepancy has been explained by assuming grain boundary diffusion dominates the overall transport process in polycrystalline $Nb_3Sn$ [39]. The high Nb regions we are reporting in these RRP® samples suggest incomplete diffusion of Sn into the centre of the grains, which is additional evidence for the dominance of grain boundary

diffusion as the primary atomic transport process during the formation of polycrystalline $Nb_3Sn$.

These high Nb volumes of the A15 phase are however metastable, and their volume fraction decreases dramatically after irradiation. We suggest that the irradiated sample will contain very high concentrations of point defects such as vacancies and antisite defects, and that these accelerate diffusion in the $Nb_3Sn$ grains, even at low temperatures, and encourages removal of the high Nb regions.

Using the GLAG theory model which predicts $B_{c2}$ as a function of bulk composition in unirradiated $Nb_3Sn$ [6, 40], the low Nb regions would be predicted to have a $B_{c2}$ of ~20 T, and the high Nb regions lie outside the bulk composition range due to their low Sn content. Therefore, it is very difficult to know how the nanoscale fluctuations may be affecting $B_{c2}$ locally because the measured value for $B_{c2}$ will be associated with the properties of the best interconnected superconducting pathway through the polycrystalline structure. Based on the microstructure of the RRP® wires, figure 7, an interconnected path can pass primarily through the low Nb regions and the grain boundaries, with the high Nb regions appearing to be discontinuous. Evidence from APT, shows that there is a larger volume of the high Nb regions in the grains for the as-received sample, which may, in this case, be contributing to the superconducting path, and producing a reduction in $B_{c2}$ compared to the irradiated sample.

However, this theory does not consider for the effects of induced radiation damage on the intrinsic properties of the volume of material comprising the interconnected current path. The observed decrease in $T_c$, of the irradiated sample, is small and could be dominated by the introduction of point defects that change the local order, but that only marginally affect the order on the scale of the coherence length in the A15 phase. This introduction of radiation induced disorder could shift the $Nb_3Sn$ from the clean limit towards the dirty limit, which may increase $B_{c2.}$ APT cannot detect these point defects but can observe larger stoichiometry changes on the nanoscale.

In addition to a reduction in the volume fraction of high Nb regions in the irradiated sample there is some evidence of stronger Cu segregation to grain boundaries. Perhaps irradiation induced vacancies are increasing Cu diffusion along the grain boundaries to the outer edge of the RRP® subelements. However, because grain boundary diffusion is already fast, the additional effect of irradiation-induced diffusion at grain boundaries is small. Grain boundaries are regions with large amounts of disorder, effectively planar non-superconducting regions which pin fluxons. We observe some evidence for a small increase in Cu concentration at the boundaries, and this may modify the pinning strength to some degree.

There is also indication of a reduction in the volume fraction and size of residual Nb nanoparticles in the irradiated sample, perhaps as a result of the excess radiation-induced vacancy concentration increasing diffusion within the grains to homogenise the A15 stoichiometry. There is strong segregation of Cu to the $Nb/Nb_3Sn$ interface which has not been reported previously. The Nb clusters in the unirradiated sample are likely acting as additional pinning sites, and the removal of them by irradiation cannot contribute to the measured increase in $F_p$.

Other features of interest which have been analysed using APT in these samples are linear features revealed by strong Cu segregation. In the as-received sample, we have detected dislocation arrays at low angle boundaries and single dislocations running out of the plane of the grain boundary. The irradiated sample contained orthogonal dislocation arrays, and a distinctive solute-decorated dislocation loop of the kind often seen in other types of neutron-irradiated materials. Cu segregation to these defects is present in both the unirradiated and irradiated material, and we do not have statistical evidence for an increase in density of features or concentration of segregated Cu after irradiation. However, the formation of decorated dislocation loops in the irradiated sample, suggested by Pande to evidence a high vacancy concentration [41], should increase the density of flux pinning sites in the irradiated sample, and may help explain the observed increase in $F_p$. Indeed, some of the *regions of disorder* previously seen by TEM in irradiated $Nb_3Sn$, and believed to contribute to the increase in flux pinning [20] could be these decorated dislocation loops.

# 5. Conclusions

Atom Probe Tomography has been used to analyse the nanoscale chemistry in as-received and fast neutron irradiated RRP® wires, and we have explored which of the observed features might help to explain the changes in their superconducting properties. The major finding is that the fine grained $Nb_3Sn$ can be split into regions with three distinct compositions; low and high Nb regions, and the grain boundaries themselves. The summed composition of these regions lies within the expected A15 area in the equilibrium $Nb_3Sn$ phase diagram, but neither the high or low Nb regions lie within the ternary equilibrium phase field. We would expect the existence of these localised compositions will control both the $B_{c2}$ and $T_c$ values within individual grains on length scales <100 nm. This work has also shown that the volume fraction of the regions of high Nb is reduced in the irradiated sample, with the overall composition lying closer to the stoichiometry that we expect to lead to higher $B_{c2}$

values. APT analysis cannot detect vacancies or localised disorder, so we are unable to comment on the extent to which the increased $B_{c2}$ value after irradiation is also likely to be caused by a reduction in mean free path. There is a reduction in $T_c$ for the irradiated sample which is likely due to induced local disorder, with the change in composition likely a much weaker effect on the $T_c$. Finally, there are additional defect structures within the irradiated sample, and enhanced segregation, which could be acting as additional pinning sites, promoting the measured increase in $F_p$.

## Acknowledgements

Work conducted at the University of Oxford was supported by the Engineering and Physical Sciences Council under grant EP/S022430/1. Work carried out at the Vienna University of Technology is within the framework of the EUROfusion Consortium, funded by the European Union via the Euratom Research and Training Programme (Grant Agreement No 101052200 - EUROfusion). Views and opinions expressed are however those of the author(s) only and do not necessarily reflect those of the European Union or the European Commission. Neither the European Union nor the European Commission can be held responsible for them.

The experiment was conceived by all authors, with the superconducting measurements conducted by T. Baumgartner supervised by M. Eisterer. Analysis of the superconducting measurements were carried out by L. Wheatley with guidance from S. Speller, M. Eisterer and C.R.M. Grovenor. APT characterisation and drafting of the manuscript were carried out by L. Wheatley with extensive discussions with all authors.

## References

[1] Ulbricht A *et al* 2005 *Fusion Eng. Des*. **73** 2-4

[2] Rossi L and Brüning O 2012 *CERN-ATS*-2012-236

[3] Ball A *et al* 2014 *CERN Technical Document FCC-1401101315-DSC* CERN

[4] Suenaga M Horigami O and Luhman T S 1974 *Appl. Phys. Lett.* **25** 624-627

[5] Charlesworth J P Macphail I and Madsen P E 1970 *J. Mater. Sci.* **5** 580-603

[6] Flükiger R Uglietti D Senatore C and Buta F 2008 *Cryogenics* **48** 293-307

[7] Suenaga M Welch D O Sabatini R L Kammerer O F and Okuda S 1986 *J. Appl. Phys.* **59** 840-853

[8] Tarantini C Balachandran S Heald S M Lee P J Paudel N Choi E S Starch W L and Larbalestier D C 2019 *Supercond. Sci. Technol.* **32** 124003.

[9] Suenaga M and Jansen W 1983 *Appl. Phys. Letts.* **43** 791-793

[10] Sandim M J R Tytko D Kostka A Choi P Awaji S Watanabe K and Raabe D 2013 *Supercond. Sci. Technol.* **26** 055008

[11] Yamashina T and Kajihara M 2006 *Mater. Trans.* **47** 829-837

[12] Cantoni M Abächerli V Uglietti D Seeber B and Flükiger R 2008 *Microsc. Microanal.* **14** 1146-1147

[13] Bett R 1974 *Cryogenics* **14** 361-366

[14] Karkin A E Arkhipov V E Goshchitskii B N Romanov E P and Sidorov S K 1976 *Physica Status Solidi (a)* **38** 433-438

[15] Brown B S Blewitt T H Scott T L and Wozniak D G 1978 *J. App. Phys.* **49** 4144-4148

[16] Fähnle M 1977 *Physica Status Solidi (b)* **84** 245-251

[17] Jenkins M L Roller G Katerbau K H and Wilkens M 1982 *J. Nucl. Mater.* **108** 603-613

[18] Pande C S 1980 Direct observation of defects in A15 compounds produced by fast neutron irradiation *Superconductivity in D- and F- Band Metals* ed H Suhl and M B Maple (Academic Press) p 349-353

[19] Holdway P and Rawlings R D 1984 *Cryogenics* **24** 137-142

[20] Pfeiffer S 2020 *PhD Thesis* TU Wien

[21] Baumgartner T 2013 *PhD Thesis* TU Wien

[22] Dew-Hughes D 1974 *Phil. Mag.* **30** 293-305

[23] Gault B Moody M P Cairney J M and Ringer S P 2012 *Atom Probe Microscopy* (Springer Science and Business Media)

[24] Tarantini C Kametani F Balachandran Heald S M Wheatley L Grovenor C R M Moody M P Su Y F Lee P J and Larbalestier D C 2021 *Sci. Rep.* **11** 17845

[25] Xu X Rochester J Lee J Y and Sumption M 2020 *Scr. Mater.* **186** 317-320

[26] Xu X Sumption M D Lee J Rochester J and Peng X 2020 *J. Alloys Compd* **845** 156182

[27] Baumgartner T Eisterer M Weber H W Flükiger R Schueuerlein C and Bottura L 2014 *Supercond. Sci. Technol.* **27** 015005

[28] Baumgartner T Eisterer M Weber H W Flükiger R Schueuerlein C and Bottura L 2015 *Sci. Rep.* **5** 10236

[29] Helfand E and Werthamer N R 1964 *Phys. Rev. Lett.* **13** 686

[30] Pfeiffer S Baumgartner T Löffler S Stöger-Pollach M Hopkins S C Ballarino A Eisterer M and Bernadi J 2023 *Supercond. Sci. Technol.* **36** 045008

[31] Tarantini C Lee P J Craig N Ghosh A and Larbalestier D C 2014 *Supercond. Sci. Technol.* **27** 065013

[32] Lee P J and Larbalestier D C 2005 *IEEE Trans. Appl. Supercond.* **15** 3474-3477

[33] Jenkins B 2019 *PhD Thesis* University of Oxford

[34] Marquis E A 2015 *J. Mat. Res.* **30** 1222-1230

[35] Welch D O Dienes G J Lazareth Jr O W and Hatcher R D 1984 *J. Phys. Chem. Solids* **45** 1225-1242

[36] Besson R Guyot S and Legris A, 2007 *Phys. Rev. B* **75** 054105

[37] Sitaraman N S Carlson J Pack A R Porter R D Liepe M U Transtrum M K and Arias T A 2019 *Phys. Rev. B* **103** 115106

[38] Kumar A K and Paul A 2009 *J. Elec. Mater.* **38** 700-705

[39] Oh S H Seol D Jeong Y J Na S H Kim J Ko W S Jeon J B and Lee B J 2022 *Acta Mater.* **234** 118050

[40] Li Y and Gao Y 2017 *Sci. Rep.* **7** 1133

[41] Pande C S 1979 *Physica Status Solidi (a)* **52** 687-696